PHYSICAL REVIEW B **82**, 165422 (2010)

Ultrathin Mn layers on Rh(001): Investigations using scanning tunneling microscopy and density functional calculations

Martin Zelený,[1,*] Fabian D. Natterer,[2,†] Albert Biedermann,[2,‡] and Jürgen Hafner[1,§]
[1]*Fakultät für Physik and Center for Computational Materials Science, Universität Wien, Sensengasse 8, A-1090 Wien, Austria*
[2]*Fakultät für Physik, Universität Wien, Boltzmanngasse 5, A-1090 Wien, Austria*

(Received 24 March 2010; revised manuscript received 6 September 2010; published 11 October 2010)

The structural and magnetic properties of ultrathin layers of Mn grown on Rh(001) surfaces have been investigated using scanning tunneling microscopy (STM) and *ab initio* density-functional calculations. STM shows perfect wetting of the Rh substrate by the first Mn monolayer (ML) accompanied by a high mobility of the Mn atoms and only little film-substrate intermixing. By way of contrast, the second monolayer is unstable against formation of multilayer islands at 300 K. However, this is only a transient effect and growth approaches a layer-by-layer mode in thicker films. At 170 K growth proceeds layer-by-layer throughout. The structure of the films is face-centered tetragonal (fct) without any indication of lateral lattice mismatch up to 20 ML thickness. The apparent height differences between terraces of different local thickness are consistent with an average axial ratio close to unity (near fcc) for 2–3-ML-thick films that decreases continuously to ≈0.94 in thicker films. Detailed spin-polarized density-functional calculations have been performed for the bulk and the (001) surface of strained fct Mn, as well as for free-standing and supported Mn/Rh(001). The results demonstrate that structure and stability of surface and thin films are strongly influenced by antiferromagnetic (AFM) ordering. In-plane $c(2\times2)$ AFM is found at the surface while bulk and the deeper layers prefer layered AFM. The calculations reproduce and explain the growth instability of 2 ML films and reproduce qualitatively the thickness-dependent variation in the film structure while the tetragonal distortion imposed by the size mismatch is overestimated because with all known exchange-correlation functionals the size ratio of bulk Rh and Mn crystals is overestimated. The calculations show that interface alloying is slightly exothermic but kinetically hindered because of a high activation energy for exchange processes.

DOI: 10.1103/PhysRevB.82.165422 PACS number(s): 75.10.Lp, 68.55.−a, 68.65.Ac, 75.70.Cn

I. INTRODUCTION

Manganese is an element with extremely complex structural and magnetic properties which exists in five allotropic forms. The α phase is cubic with 58 atoms in the unit cell (space group $T_d^3-I\bar{4}3m$) at ambient conditions, stable up to 1000 K. At a Néel temperature of $T_N=95$ K, α-Mn undergoes a paramagnetic to antiferromagnetic (AFM) transition accompanied by a tetragonal distortion of the crystal structure.[1] The AFM structure of α-Mn is noncollinear, with large magnetic moments (up to 3 μ_B) on sites I and II, and much smaller moments on the remaining positions. β-Mn is cubic with 20 atoms in the unit cell (space group $P4_132$),[2] stable between 1000 and 1368 K. A face-centered cubic γ phase exists between 1368 and 1406 K, a body-centered δ phase from 1406 K up to the melting point at $T_M=1517$ K. High-pressure studies[3] have revealed a transition to a hexagonal close-packed ϵ phase at about 165 GPa. The properties of the allotropic phases of Mn have been studied using density-functional theory (DFT).[4,5] It has been demonstrated that the complex noncollinear antiferromagnetism of α-Mn arises from the conflicting tendencies to simultaneously maximize bond strength (as expected for a half-filled d band) and the magnetic moment (according to Hunds rule). The magnetically ordered states of the cubic phases of Mn are unstable against tetragonal distortion. In face-centered γ-Mn a tetragonally contracted phase ($c/a=0.945$) with layered type-1 (CuAu-type) AFM (Ref. 6) and a tetragonally expanded state ($c/a=1.048$) with (001) in-plane AFM are energetically almost degenerate.[7] For body-centered δ-Mn multiple minima representing metastable spin-spiral states with energies slightly lower than the energetically most favorable collinear $c(2\times2)$ in-plane antiferromagnetic phase have been identified.[7,8]

The Mn polymorphs differ not only in their crystalline and magnetic structures: substantial differences in the atomic volumes demonstrate large magnetovolume effects. For α-Mn an experimental atomic volume of 12.05 Å^3 has been measured by Lawson *et al.*[1] For γ-Mn the lattice parameters of $Mn_{96}Cu_4$ alloys measured at room temperature ($a=3.795$ Å, $c=3.59$ Å, Ref. 9) yield a larger atomic volume of 12.92 Å. The large volume difference of 7.3% is correlated with different magnetic properties: as discussed above, α-Mn may be considered as a topologically close-packed compound formed by high- and low-spin Mn atoms while in γ-Mn all Mn atoms have a large magnetic moment of about 2.4 μ_B.

DFT calculations on slabs representing the (001) surfaces of the locally stable phases of tetragonal Mn predicted strongly enhanced magnetic moments reaching about 3 μ_B. For the nearly bcc ($c/a=0.684$) and expanded fcc ($c/a=1.049$) phases the in-plane AFM stable in the bulk was found to extend to the surface. For the tetragonally contracted phase with layered AFM, a reduced surface energy was reported if in the surface layer the magnetic moments adopted in-plane AFM.[7]

The magnetic properties of the high-temperature allotropes can be studied experimentally in quenched samples, by extrapolating the data acquired on Mn alloys to zero impurity concentration, or in thin films stabilized by epitaxial growth.

The layered AFM of γ-Mn below a Néel temperature of $T_N = 570$ K, coupled to a tetragonal distortion with $c/a = 0.946$ has been confirmed by Endoh and Ishikawa[9] in a study of Fe-Mn alloys doped with about 4 at. % Cu to stabilize the fcc phase. Mn films grown on a number of fcc substrates [Cu,[10] Ag,[11] Pd,[12] and Ir (Ref. 13)] assume a strained face-centered tetragonal structure with $c/a < 1$. For low-temperature grown films where interdiffusion is suppressed, experiment and theory[14–16] agree on in-plane $c(2\times2)$ AFM in the monolayer limit and layered AFM in multilayer films. High-temperature growth or annealing of low-temperature grown films leads to the formation of ordered alloys with a $c(2\times2)$ structure and a ferromagnetic (FM) coupling between next-nearest-neighbor Mn atoms in the interface layer. The predicted existence of a tetragonally expanded γ-Mn with $c/a \sim 1.05$ and in-plane AFM was confirmed by Kohlhepp *et al.*[17] for thin films grown on strained face-centered tetragonal Co(001) [stabilized in turn by epitaxial growth on Cu(001)].

Most investigations of the growth of Mn films on body-centered cubic substrates have concentrated on Mn/Fe(001). For a detailed discussion of the abundant literature up to 2005 we refer to our earlier work.[7] Using spin-polarized scanning tunneling microscopy Yamada *et al.*[18] showed that Mn films grow in a body-centered tetragonal phase with $(c/a)_{bct} = 1.11$, multilayer films adopt a layered antiferromagnetic order. Schlickum *et al.*[19] studied the magnetic structure of Mn films grown on stepped Fe(001) surfaces. In the regions where the Mn film overgrows a step in the substrate a frustration of the layered AFM order occurs, leading to the formation of a domain wall whose thickness increases in proportion to the thickness of the Mn film. Grazioli *et al.*[20] demonstrated that the frustration arising from the competition between the FM coupling at the interface and the AFM coupling in the Mn film is most evident in the monolayer and bilayer limit where a "spin-flop" structure with an almost perpendicular orientation between the moments in a $c(2\times2)$ ordered Mn film and those of the Fe substrate has been found by x-ray magnetic circular dichroism and linear dichroism spectroscopies. bct Mn/Fe(001) films grow only up to a critical thickness of 10–20 monolayers, and a structural transition to α-Mn films has been proposed for thicker films.[21,22] Gao *et al.*[23] have demonstrated using low-energy electron diffraction (LEED) and spin-polarized STM that beyond the critical thickness Mn films reconstruct with a $(\sqrt{10}\times2\sqrt{10})R18.4^\circ$ periodicity (corresponding to a surface unit cell twice as large as that of α-Mn) and shows a noncollinear spin-arrangement. DFT calculations[7] have confirmed that the strongly enhanced surface magnetic moments stabilizes a slightly noncollinear spin-flop structure with $c(2\times2)$ periodicity in monolayer and bilayer films. Up to a thickness of 6 ML, the stable magnetic configuration of the films is predicted to consist of a $c(2\times2)$ ordered AFM surface layer, reduced magnetic moments in the following two subsurface layers, and layered AFM in the deeper layers with magnetic moments which are about half as large as those in the surface layers. The geometric structure of the films is characterized by strong relaxation effects influencing even deeper layers dominated by strong local magnetovolume effects. However, it must be noted that the in-plane AFM of the surface layer has not yet been experimentally confirmed. The properties of Mn films grown on body-centered tungsten surfaces are determined by the large size mismatch and the strong chemical interaction across the surface.[24,25] Mn/W(110) films show $c(2\times2)$ in-plane AFM for up to 3 ML and layered AFM in thicker films. Mn/W(001) films are predicted to be FM up to 2 ML, the ferromagnetism being induced by the strong hybridization between the Mn and W d bands across the interface. Recent spin-polarized scanning tunneling microscopy has shown, however, that the magnetic order of 1 ML Mn/W(100) films is a long-period spin-spiral stabilized by spin-orbit coupling.[26] The unexpected noncollinear spin-structure of Mn/W(001) films adds to the complexity of the magnetic properties of tetragonal Mn films caused by the competition between AFM and FM exchange interactions (both within the film and with the moments of an eventually magnetically ordered substrate), strains imposed by pseudomorphic growth and chemical interactions across the interface.

The investigation of Mn films grown on Rh(001) substrates is motivated by the following observations: (i) there is a modest size mismatch between the atomic volume of Rh (13.73 Å^3) and Mn [α-Mn: 12.05 Å^3 (Ref. 1), γ-Mn: 12.92 Å^3 (Ref. 9)]. The size mismatch for γ-Mn (0.941) deviates only 0.5% from the equilibrium axial ratio $c/a = 0.946$,[9] i.e., there should be no lateral misfit between thicker Mn(001) films and Rh(001) substrate if the Mn behaves like γ-Mn. (ii) At temperatures above 1100 K Rh is soluble in γ-Mn up to about 32 at. %. At lower temperatures ordered intermetallic compounds are formed (γ' Mn_3Rh phase with the Cu_3Au structure, β-RhMn with a broad homogeneity range from 35 to 55 at. % Rh),[27] indicating a certain tendency toward intermixing. (iii) The size-mismatch for Mn/Rh(001) is comparable to Mn/Cu_3Au(001) where a change from nearly ideally fcc Mn to a tetragonally contracted structure is observed in dependence of film thickness.[28,29]

The investigations are based on scanning tunneling microscopy (STM), Auger electron spectroscopy (AES) and *ab initio* density-functional calculations. We will first describe in Sec. II the techniques used in the experimental investigations and discuss their results. In Sec. III we shall first review the computational setup and discuss the choice of an appropriate exchange-correlation functional, followed by the presentation of the theoretical results for the structure and magnetic properties of strained tetragonal Mn in a bulk phase, at the free surface and in thin films grown on Rh(001) substrates. The final chapter is devoted to a critical confrontation of theory and experiment.

II. EXPERIMENT

A. Instrumentation and sample preparation

The experiments were carried out using a variable temperature STM (Omicron VT-SPM) mounted in an ultrahigh-vacuum chamber at typical pressures of 1×10^{-10} mbar. The Rh(001) substrate initially was cleaned by prolonged simultaneous sputtering with 1 keV Ar$^+$ ions and cycling the temperature between 770 and 1070 K to reduce surface carbon.[30]

The preparation immediately preceding the experiments was sputtering at ≈1020 K followed by a few minutes annealing at the same temperature. The Mn films were grown by molecular beam epitaxy from Mn flakes (99.99%) in a W crucible heated by electron bombardment, at a rate between 0.05 and 0.3 ML/min. The substrate temperature during growth was 150–170 or 300 K. For control experiments, Mn ions were blocked by applying +1.2 kV to the evaporator exit tube during film growth but no effect on the films was observed. The average film thickness t of thinner films was determined by monitoring the progress of layer completion by STM (but with the tip fully withdrawn during deposition) resulting in an accuracy of 0.1 ML. Thicker films, showing step flow obscuring the position of the substrate step edges, were grown by extrapolating the deposition time based on the actual growth rates of the thinner films. Subsequently, t was checked by AES using a layer model and attenuation lengths[31] for Fe (instead of Mn) and Rh. Surface purity was determined by AES with a sensitivity of about 0.3% of the unattenuated Rh-303-eV peak corresponding to a few percent surface coverage of C or O. While no O-512-eV peak was detectable by AES (after subtraction of the small Mn-512-eV component), the estimated C coverage based on the C-275-eV peak was about 5% on average in agreement with atom counting in the STM images.

B. Quantitative STM

Using the STM to quantitatively measure vertical height differences such as monoatomic step heights or multilayer island heights is problematic but facilitates the measurement of locally varying interlayer distances. Since STM height differences contain both geometric and electronic contributions, they are conventionally termed “apparent” step heights. In special cases, however, they do reflect actual height differences fairly accurately: For instance, monoatomic step heights are free of electronic contributions if the electronic and geometric surface structures on either side of the measured step edge are equal. This condition is fulfilled if (i) film interface and surface are sufficiently independent and therefore surface relaxations on either side cancel (and the same for interface relaxations) and (ii) anomalous spectral features such as standing waves between surface and interface can be excluded in the relevant energy range (here 0–1 eV below the Fermi edge). In these cases, the measured step height corresponds to the *bulk* interlayer distance of the film by definition while *surface* interlayer distances are not accessible. In other cases, such as very thin films, where a violation of above condition is likely, I/V and I/z spectra may be consulted to estimate the magnitude of electronic contributions. Apparent height differences corrected for the scanner sensitivity are obtained by normalizing the measured height differences h to the measured substrate step height h_{Rh}, which is an accurate measure of the Rh bulk interlayer distance and Rh lattice constant.

In order to achieve sufficient precision, all height values of a given terrace were averaged, after masking regions of ill-defined height such as surface defects or the very step edges. For a fully automated and objective evaluation of surface averaged step heights, a compensation method was used: first, the image is segmented based on the monolayer height level and then each terrace is shifted up or down by adding an integer multiple of a trial step height h_t, effectively leveling the entire surface. Then a high-pass filter is applied to remove the background. If the trial-step height differs from the true-step height, the residual discontinuity along the former step edges survives the high pass filtering and is quantified by calculating the residual standard deviation σ of the entire image. Minimizing $\sigma(h_t)$ yields the step height h.[32] The statistical error is estimated by partitioning each image into nine smaller images and applying the procedure on each of them and, if available, calculating the weighted average from several equivalent images. For instance, the such determined ratio of step heights measured on Cu(001) and Rh(001) substrates of $0.956 \pm 0.5\%$ agrees with the known bulk ratio $a_{\mathrm{Cu}}/a_{\mathrm{Rh}}=0.950$ at 300 K (Ref. 33) with acceptable precision.

In order to detect lateral lattice mismatch in the films, the surface lattice constant a was determined by measuring the interatomic distance averaged over image widths ≥15 nm and normalizing it to that of the Rh substrate measured with the same tunneling tip. The determination of the lateral lattice parameter is possible without image deskewing if lattice vector combinations parallel to the fast scan direction are evaluated, which are not affected by the slow drift motion between tip and sample, best done in the Fourier transformed (FFT) image. Since in the absence of surface defects such as monoatomic steps the image size is the only limitation of the periodicity, the peaks in the FFT image have near pixel sharpness, and are evaluated by calculating the center of gravity of the largest pixel and its eight neighbor pixels. For the square lattice the surface parameter is $a=[k_{f,(01)}^2+k_{f,(10)}^2]^{-1/2}$ with the components of the (10) and (01) reciprocal lattice vectors in the fast scanning direction. The precision is then limited only by the short term reproducibility of the scanning speed mainly determined by the drift of the piezo constants. From repeated measurements of the substrate lattice constant, it was determined that this drift is below 1% on the scale of days for our STM, at least if the temperature of the STM while measuring the reference lattice and the actual sample is the same.

C. Submonolayer films

For films grown at 300 K, we find that the first ML covers the substrate completely before any second ML islands nucleate. Even at 170 K the first ML is more than 90% complete at this point. A detailed account of the Mn-Rh alloying in the initial ML will be published in a separate paper but we summarize here the relevant details: although the existence of intermetallic Mn-Rh compounds[27] in general and our calculations (cf. Sec. III C 3), in particular, indicate a substantial driving force for alloying, we see surprisingly little alloying in the initial Mn monolayer, which is evidence of a sizeable barrier for surface-subsurface exchange processes. A homogenous surface alloy forms only on heating above 500 K as seen by temperature programmed AES followed by final state STM. We see a decrease of the Mn signal at 700 K

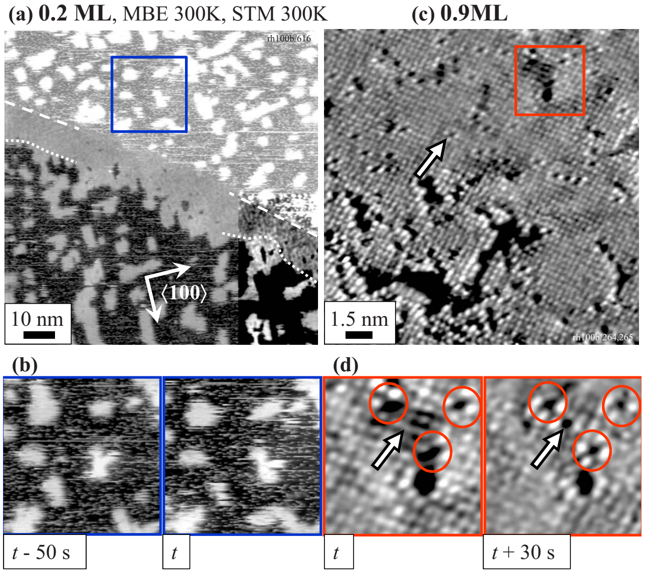

FIG. 1. (Color online) (a) STM image (−1 V, 0.1 nA) of 0.2 ML Mn/Rh(001) with a single monoatomic substrate step edge crossing the image (dashed line). At the step edge, a narrow surface alloy seam is formed (between dotted and dashed line) showing a pattern of brighter Mn- and darker Rh-rich regions (contrast enhanced detail in lower right corner). The step edges of the Mn islands on the terraces are preferentially aligned along ⟨100⟩-type directions (white arrows). (b) Subsequent images of detail showing shape fluctuations of the Mn islands. (c) Atomically resolved STM image (−0.11 V, 0.1 nA) of the almost completed first Mn ML showing individual vacancies (arrow). Atomic corrugation is 10 pm on average. (d) Subsequent images of detail showing the "appearance" of a fourth vacancy (arrow) between three others (circles).

to about 80% of its initial value accompanied by the formation of a (2×2)-Mn_3Rh surface alloy. Inhomogeneous alloying occurs already at 300 K near step edges via two-dimensional mixing [cf. Fig. 1(a)], leading to narrow Mn-Rh alloy seams with an estimated Rh concentration around 50%. Due to the high Mn mobility (see next paragraph) during sub-ML growth, further distribution of the Rh atoms leading to a homogeneous, dilute surface alloy is possible depending on the growth conditions. For our typical terrace widths of 50–100 nm (0.1° miscut) the average Rh concentration in the completed first monolayer is 5–10 %.

A remarkable property of sub-ML Mn films is the weak two-dimensional cohesion. The resulting Mn atom mobility causes fluctuating island step edges appearing frayed in the images [Fig. 1(b)]. In addition, the island edges are preferentially aligned along ⟨100⟩-type directions, which is also rather unusual as this is a very open step edge type with every edge atom having only two nearest Mn neighbors. Moreover, Fig. 1(c) shows that nearly completed monolayer films contain an appreciable density of single vacancies [≈3% in Fig. 1(c)], and the total density including mobile vacancies may be even higher, as some of the vacancies were seen to fluctuate [Fig. 1(d)].

D. Growth modes and 2 ML instability

In contrast to the first ML, the cohesion of Mn atoms in the second ML is higher, and the island edges are sharp [Fig. 2(a)]. Above 1.5 ML average thickness, however, the monoatomic islands on top of the closed first ML typically stop to grow and start to shrink again, while double height islands grow on the terrace below forming a locally 3 ML thick film [Fig. 2(b)]. These islands form right at the step edge and therefore second ML atoms can migrate without having to cross a double height step edge, i.e., low-barrier diffusion pathways seem to be essential for this phenomenon to occur at 300 K. Sometimes these double height islands extend over the entire terrace and form triple height or even higher islands on the next terraces, in particular in regions where step edges approach each other. Atomically resolved images of the double height island surface do not show a significant change in the atomic structure or lateral lattice constant. Further deposition of Mn does not result in a pronounced three-dimensional-island growth on the wetting layer (Stranski-Krastanov growth) but the multilayer islands grow both in width and height and eventually coalesce and film growth proceeds in a step-flow mode.

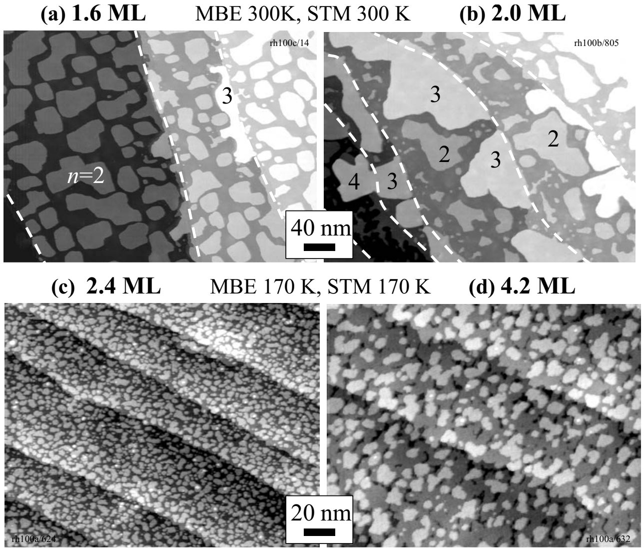

FIG. 2. Second ML instability at 300 K and near perfect layer-by-layer growth at 170 K. (a) STM image after growth at 300 K sample temperature (1.6 ML, −2.1 V, 0.14 nA). The dashed, white lines outline the substrate step edges. The numbers in the images indicate the local integer film thickness *n* in ML. A few double height ($n=3$) islands can be seen nucleating right at the step edges on the lower terrace. (b) STM image (2.0 ML, −1.0 V, 0.13 nA). Compared to the 1.6 ML film, the single height island coverage ($n=2$) is significantly reduced and the double and triple height ($n=3,4$) island coverage increased. [(c) and (d)] STM images after growth at 170 K (−1 V, 0.1 nA and −1.9 V, 0.1 nA).

However, the precise film morphology for growth at 300 K varies. Decreasing the growth rate (below 0.1 ML/min) and increasing surface contamination can partially or even fully suppress the instability. It is conceivable that the width of the alloy seams near the step edges and the exact Rh distribution in the wetting layer influence the nucleation of the multilayer islands. In those cases showing the instability, the closing of the film may occur anywhere between 3 and 20 ML. Growth at 300 K with rates >0.2 ML/min and typical contamination levels always leads to the instability and it

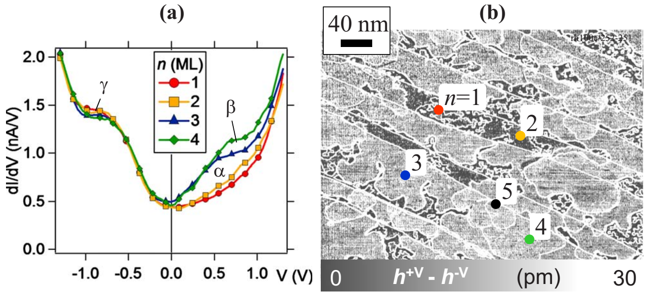

FIG. 3. (Color online) (a) Tunneling spectra in dependence of local integer thickness n of a 2.2 ML film with the tunneling distance set at -1.5 V and 0.13 nA. Greek letters indicate spectral features referred to in the text. (b) Difference between STM images of 2.9 ML Mn/Rh(100) acquired with positive and negative sample voltage (± 1 V, 0.1 nA). The white lines outline areas of constant n. A corresponding image of the local thickness at the same site is shown in Fig. 4(b).

takes comparably longer until the second ML closes.

Layer-by-layer growth is reproducibly achieved for sample temperatures of 150–170 K [Fig. 2(c)]. Subsequent annealing to 300 K increases island sizes and closes the small holes in the completed monolayer. In these cases, the metastability of the completed second ML becomes apparent only after heating to about 360 K. At this temperature monoatomic holes (locally 1-ML-thick film) and monoatomic islands (locally 3-ML-thick) form side by side on the terraces. In contrast, 2.8-ML-thick films grown at 170 K are stable even when heated to 430 K.

The locally varying integer thickness n in films showing the 2 ML instability provides the opportunity to determine the n-dependent tetragonal distortion, i.e., the layer averaged ratio of vertical and lateral lattice constant $\overline{c/a}$ from the local apparent height of the Mn film. In order to estimate the magnitude of electronic contributions to the apparent height, we first discuss the I/V and I/z spectra. Figure 3(a) shows dI/dV spectra of a 2.2 ML film in dependence of local thickness n. The spectra $n=1,2$ and $n=3,4$ are separated by a large spectral feature α that just reaches the Fermi edge. A smaller feature β confined to energies larger than 0.5 eV above E_F distinguishes $n=3$ and 4. The feature γ at $E_F - 1$ V is much weaker as expected due to the exponential suppression of the sample density of states (DOS) below E_F. The quantitative effect of these features on a height measurement can be seen in difference images $h_n^{+V}-h_n^{-V}$ between positive and negative tunneling voltages [Fig. 3(b)]. A comparably large difference of about 15 pm is seen between $n=1,2$ and $n\geq 3$ corresponding to spectral feature α. This feature, however, is centered above the Fermi edge and should have less effect on height measurements at negative voltages. The small difference in the sample DOS above E_F distinguishing $n=3$ and $n=4$ does have a noticeable effect (3–5 pm) in the difference image but is clearly not relevant for the negative sample voltages used in the height measurements. For $n>3$, the difference image does not show any significant height differences.

I/z spectra, that can indicate changes in the local work function, show no significant deviations except for the second layer, which appears to have a 0.2–1 % shorter decay length κ than the other layers, and therefore may appear slightly deeper by $z_0\Delta\kappa/\kappa\approx 1-5$ pm in the images, presuming an exponential tunneling law with a tunneling distance z_0 of 500 pm. Such a change is consistent with a small work function increase due to the higher C coverage observed on the residual second ML islands [cf., e.g., C/Ni(001) (Ref. 34)]. Carbon coverage is higher on the second ML because at 300 K the C atoms do not accompany the Mn atoms during the decay of the second ML but remain on the 2 ML islands and stabilize them causing the skeletal island shapes of the small residual second ML islands [cf. Fig. 2(b)].

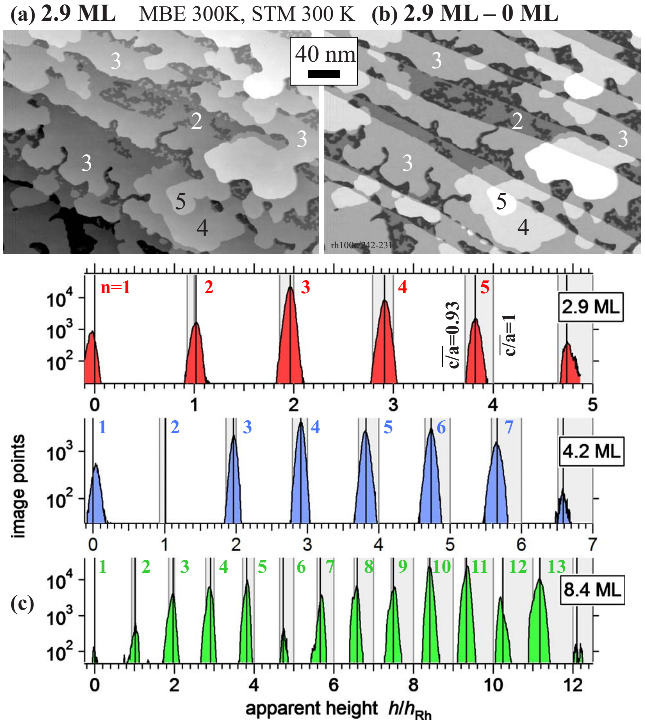

FIG. 4. (Color online) Layer averaged apparent axial ratio in dependence of local thickness n. (a) STM image (-1.0 V, 0.1 nA) of a 2.9 ML film. (b) Same image with an image of the substrate at the same site subtracted (cf. text). (c) Histograms of the above 2.9 ML difference image and of similar difference images at higher average thickness. The vertical lines mark the positions of the maxima (height levels n) common to all three histograms. The gray areas mark the range of the respective height level n expected for films with an average axial ratio between 0.93 and 1. The half width of the peaks for $t=2.9$ is about 6 pm or 0.03 normalized (note the log. scale of the vertical axis).

To measure the n-dependent apparent heights of the Mn film with highest precision, an image of the substrate at the exact same position is subtracted [Figs. 4(a) and 4(b)]. This is done by leveling both images and using Rh surface defects visible in both images to laterally align both with nanometer precision using elastic registration.[35] Finally, a median filter with 1 nm (2 pixel) radius was applied to reduce image noise. In Fig. 4, histograms of the apparent height level h of such prepared images are shown for three different average thicknesses t. A 4-nm-wide band along the step edges is excluded from the histograms. All levels n can be aligned quite well when comparing the three histograms except the first level $n=1$, which differs a little. The positions of the maxima in the histograms are equal to $n-1$ times the apparent axial ratio averaged over all film layers except the distance between substrate and first Mn monolayer. In the histograms the axial ratio range (0.93–1.00) is indicated for each height level, which reveals the evolution of the average axial ratio with increasing integer thickness n. Including the distance between substrate and first Mn monolayer in the layer averaging would lead to average axial ratios $(\overline{c/a})_n$ that are only slightly different.

Based on the histogram of the 8.4 ML film, it is clear that the axial ratio for large n must be close to 0.93 regardless of the precision of the apparent height of the reference level $n=1$. The question concerning the axial ratio for small local thickness n is more subtle because the height of level $n=1$ is not arbitrarily precise as shown in the above discussion of the dI/dV spectra. If we assume that the apparent height of the wetting layer is a valid reference, the histogram maxima in Fig. 4(c) indicate a fairly smooth transition of the axial ratio between the 1.00 and 0.93 between 2 and ≈8 ML. However, on assuming that the level $n=1$ is inaccurate because of electronic effects, and rigidly shifting the histograms by about 20–30 pm toward smaller values, a reasonably good fit is obtained with all layers above the wetting layer having an axial ratio of 0.91–0.92.

For at least two reasons the first interpretation is preferred: (i) shifting the histogram requires the assumption that the apparent height of level $n=1$ contains electronic contributions corresponding to more than 20 pm compared to levels $n>1$, which is not very likely considering the above discussion of the tunneling spectra. (ii) The Mn atomic volume determined by LEED-I/V by Schirmer and Wuttig for 5.2 ML Mn/Cu$_3$Au films,[28] is 0.98 relative to that of Rh, which is consistent with or even larger than that obtained from the histograms in Fig. 4(c).

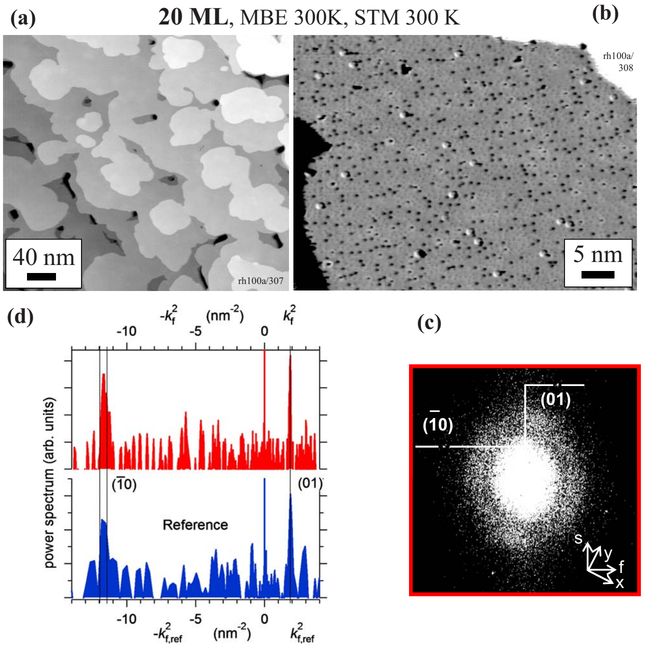

FIG. 5. (Color online) (a) Overview (−1 V, 0.1 nA) and (b) high-resolution STM images (−0.7 V, 0.1 nA) of 20 ± 3 ML Mn/Rh(001) showing impurity atoms (very likely O, 2% coverage by counting) as dark spots and C atoms (6%) as much weaker spots sparsely decorating the Mn lattice. The small number of larger bright spots are due to an unknown species. (c) Fourier transformed image of the "O" spots revealing the first-order peaks of the underlying Mn lattice. (d) Upper curve: profile through Fourier transformed image along the kinked line plotted against the square of the wave number to facilitate direct comparison of $1/a^2=k_{f,(01)}^2+k_{f,(10)}^2$ with a Rh(100) reference image (lower curve). The pair of vertical lines on both sides of the ($\bar{1}$0) peak indicate ±1% uncertainties in the lattice parameter a (≈±2% for $1/a^2$).

E. Closed films up to 20 ML thickness

Closed films were obtained either (i) by growth at 150–170 K and annealing to 300 K, or (ii) by suppressing/weakening the 2-ML instability directly at 300 K, typically achieved by very low growth rates between 0.05 and 0.1 ML/min. Whether the epitaxial condition $a_{\mathrm{Mn}}=a_{\mathrm{Rh}}=0.269$ nm is met is checked by inspecting the surface of a 20 ML film for misfit reconstructions. To compensate a misfit of $\varepsilon=1\%$, the distance between interface dislocations must be at least $a_{\mathrm{Rh}}/\varepsilon=27$ nm. Possible candidates that can form without long-range mass transfer are either interface dislocations with out-of-plane Burgers vectors revealing themselves by crystallographically aligned step edges on the surface[36] or stacking fault wedges.[37,38] The latter are structurally similar to bulk stair-rod dislocations[38] with the partial dislocations replaced by pairs of 1/3- or 2/3-height surface steps (about 60 or 120 pm high) laterally separated by a few nanometer causing tell-tale bright or dark stripes. Both steps or stripes are completely absent in our STM images [cf. Figs. 5(a) and 5(b) using the dark impurity atom spots, about 60 pm deep, as height reference]. Moreover, the direct measurement of the surface lattice constant using the sharp peaks in the Fourier transformed image [Figs. 5(c) and 5(d)] results in a Mn lattice parameter at the surface that deviates only by −0.2 ± 1.3% from that of the substrate lattice. Therefore it is clear that the films are fully epitaxial at least up to 20 ± 3 ML thickness.

To probe the average interlayer distance and by that the average axial ratio $\overline{c/a}$ and atomic volume, the apparent heights of monoatomic, substrate-uncorrelated surface steps were measured [Fig. 6(a)]. In films grown by two-dimensional island nucleation [cf., e.g., Fig. 2(a)] this corresponds to the measurement of the apparent height of monoatomic islands (or holes), which after annealing to 300 K are typically about 5–20 nm wide. Since the measurement of island heights and hole depths produces consistent results, large effects from lateral electronic confinement in small islands are unlikely. However, an effect of the high density of step edge atoms on the film structure cannot be excluded.

Above 10 ML thickness, step flow dominates (islands larger than terrace width) and the step height becomes independent of thickness. This indicates that the effects of surface and interface on the interlayer distances are now sufficiently decoupled and the apparent step height may be used to quantitatively determine the axial ratio $(c/a)_{\mathrm{bulk}}$ of the film bulk layers (cf. Sec. II B). We obtain $(c/a)_{\mathrm{bulk}}=0.94\pm0.02$,

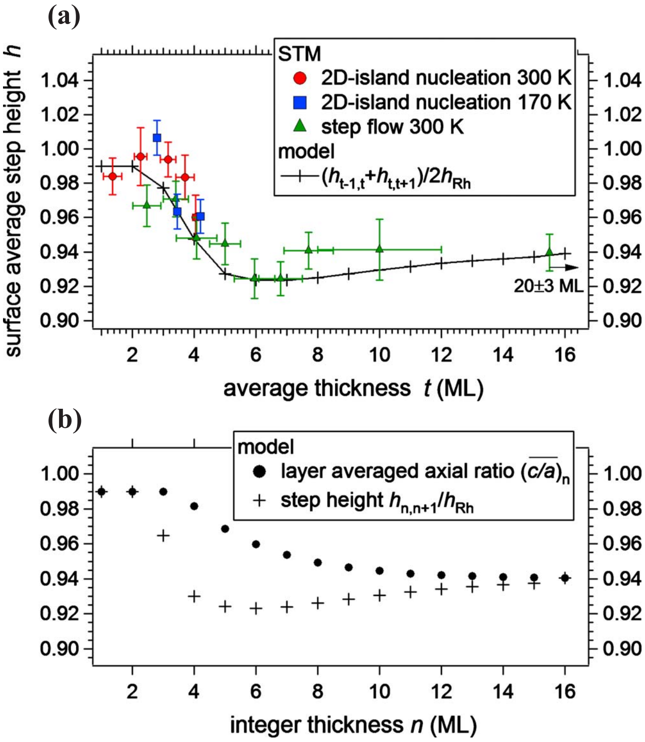

FIG. 6. (Color online) (a) Surface average of the apparent step heights measured by STM in dependence of the average film thickness t for different growth modes and growth temperatures. The error bars shown are the statistical errors only. Also shown is the step height corresponding to the model thickness dependence shown below. Since in a closed film with step edges uncorrelated with those of the substrate the local thickness shows at least three levels, subsequent step heights $h_{n-1,n}$ and $h_{n,n+1}$ of the model are averaged with $n=t$. (b) Relation of step height $h_{n,n+1}$ and layer averaged axial ratio $\overline{(c/a)}_n$ for an exponential decrease in the axial ratio above $n=3$ that roughly fits the experimental data.

which is also the atomic volume of Mn relative to that of Rh because the films are strictly epitaxial. This value is close to the value found in multilayer islands for large n described in the previous section (0.93, Fig. 4). Almost exactly the same Mn volume (relative to that of Rh) has been found for Mn/Ir(001) superlattices with 5–11 ML Mn and 1–11 ML Ir sublayers (0.93–0.96, extended x-ray absorption fine-structure analysis),[13] 10 ML Mn/Pd(001) films (0.94, LEED-I/V),[12] and for quenched bulk $Mn_{96}Cu_4$ (0.94).[9]

The $(c/a)_{\mathrm{bulk}}$ ratio may be also used to estimate the lateral film strain with respect to the fct Mn equilibrium phase. In most (001) oriented metal crystals, biaxial in-plane strain ε_a causes a change in the tetragonal ratio c/a that is 2–3 times higher (factor $1+2c_{12}/c_{11}$) with bulk fcc Mn closer to 3 (volume conserving tetragonal distortion) based on the results of the calculations presented in Sec. III B. As the equilibrium axial ratio for this type of fct Mn is around 0.94–0.95,[7,9] and we find 0.94 ± 0.02, ε_a cannot be larger than 1% in our Mn/Rh(001) films.

Similar to the findings in the previous section, deviations of the apparent step height from these "bulk" values were detected below 7 ML thickness. Monoatomic step heights, however, are not directly meaningful in very thin films where surface-independent film "bulk" layers do not exist. In these films, the general dependence of the normalized monoatomic step height $h_{n,n+1}/h_{\mathrm{Rh}}$ (between locally n- and $n+1$-ML-thick films) on the layer averaged axial ratio $\overline{(c/a)}_n$, $h_{n,n+1}/h_{\mathrm{Rh}} = (n+1)\overline{(c/a)}_{n+1} - n\overline{(c/a)}_n$ must be considered. Figure 6(b) shows a possible $\overline{(c/a)}_n$ curve that roughly reproduces the step height curve observed experimentally. Note the characteristic minimum in $h_{n,n+1}$, that is sharp for abrupt changes in the interlayer distance but can be very shallow for continuous changes. These $\overline{(c/a)}_n$ values are also very similar to those that can be seen in the height histograms of the open films in Fig. 4(c).

III. THEORY

A. Computational setup

The quantum-mechanical framework of our investigation is density functional theory. The calculations performed in this study used the VASP (Vienna *ab initio* simulation program) code.[39] This program performs an iterative solution of the Kohn-Sham equations for periodic boundary conditions. The electronic orbitals are expanded in terms of plane waves with a maximal kinetic energy of 330 eV. The electron-ion interaction is described by projector-augmented wave (PAW) potentials.[40,41] The PAW approach shares the computational efficiency of the pseudopotential approach but is an all-electron technique avoiding the problems related to the linearization of the core-valence exchange interaction.

The Mn/Rh(001) system has been modeled by slabs comprising ten Rh layers, one to six Mn layers, and sufficiently thick vacuum space of 15 Å. Slabs consisting of up to twenty Mn layers have been used to model Mn surfaces. For both FM and AFM (layered and in-plane) configurations we used slabs with $c(2\times 2)$ surface cells, i.e., with two atoms per layer. VASP allows to calculate the Hellmann-Feynman forces acting on ions hence a full structural optimization of the film/substrate complex may be carried out. The structural relaxation is completed after all forces, except those acting on atoms in the five frozen layers at the bottom of the slab, drop below 10 meV/Å. Brillouin-zone integrations have been performed via the Methfessel-Paxton technique[42] with a smearing parameter of 0.2 eV and all total energies were extrapolated to zero smearing. We used a mesh of 100 irreducible k points for the surface- and thin-film calculations and 200 k points for bulk calculations. The surface stress was calculated according to the procedure proposed by Fiorentini and Methfessel.[43] Local magnetic moments have been calculated by integration of the spin-densities over atomic spheres using a site-independent radius of 1.33 Å and 1.40 Å for Mn and Rh, respectively.

The calculations have been performed with the gradient-corrected exchange-correlation functional due to Perdew, Burke and Ernzerhof[44] predicting lattice constants of 3.821(3.800) Å for Rh and 3.563(3.724) Å for γ-Mn (experimental values[45] in parentheses). Earlier investigations[16,46] have shown that using a local exchange-correlation functional a nonmagnetic ground state is predicted for fcc Mn while calculations with a gradient-corrected functional yield the correct antiferromagnetic

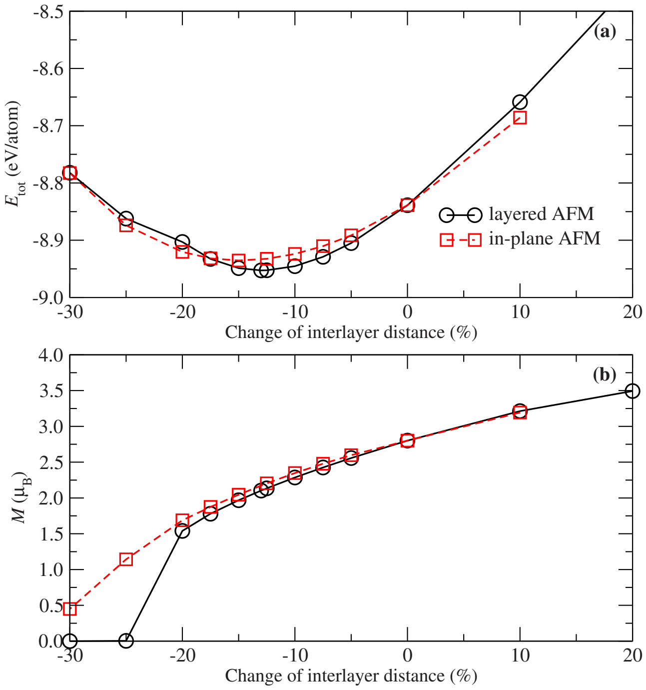

FIG. 7. (Color online) Total energy and magnetic moment of tetragonal Mn constrained to match the in-plane lattice constant of a Rh(001) surface as a function of the change of the interlayer distance with respect to fcc Rh (in %). Both layered and in-plane $c(2\times2)$ antiferromagnetism have been considered.

ground state. It is necessary to emphasize that with all currently available exchange-correlation functionals[44,47–49] DFT leads to a larger size mismatch (6.8%) than experiment (2%).

B. Strained tetragonal Mn-bulk, surface, and free-standing slabs

Figure 7 shows the total energy and magnetic moment for the layered and $c(2\times2)$ in-plane antiferromagnetic phases as a function of the interlayer distance d. Both phases are contracted by an amount (Δd=13.0% compared to fcc Rh for the layered AFM phase, and by 14.9% for in-plane AFM) which is lower than expected under volume conservation (Δd ~20%). The expanded atomic volume is reflected in an absolute value of the magnetic moment increased to about 2.1 μ_B (compared to 1.7 μ_B for in-plane and 1.4 μ_B for layered AFM upon volume relaxation at a fixed axial ratio of c/a=0.8).[7] At equilibrium, layered AFM is preferred by 17 meV/atom over in-plane magnetic ordering. $c(2\times2)$ in-plane AFM is energetically preferred only for tetragonally expanded Mn. To understand the change in the stability of the AFM phases one has to remember that $c(2\times2)$ AFM in the (001) plane corresponds to layered AFM in the (100) planes—for a cubic crystal structure both magnetic phases are equivalent.

The surface of strained tetragonal Mn has been modeled by slabs with eight to twenty monolayers. The in-plane lattice constants are always fixed to match a Rh(001) surface while the interlayer distances are relaxed for the five top-layers. Layer AFM, in-plane $c(2\times2)$ AFM and a mixed AFM configuration with in-plane ordering in the surface layer and layered AFM in the deeper layers have been considered. The structural and magnetic properties of the Mn(001) surface, as calculated for a 20-layer slab are summarized in Table I. For all magnetic configurations the absolute values of the surface moments are enhanced to about 3.3 μ_B and show an oscillatory convergence to their bulk values within a few atomic layers. The surfaces are under considerable compressive stress. While the surface stress is isotropic for layered AFM, it is strongly anisotropic for in-plane AFM. A high surface stress is found along the [010] direction, corresponding to an AFM coupling between FM-ordered (010) planes, while the stress almost vanishes for the [100] direction along which $c(2\times2)$ AFM ordered planes alternate. This is a manifestation of the strong magnetostructural effects characteristic for Mn. For this thick slab layered AFM is preferred over in-plane AFM but a mixed AFM phase with in-plane order in the surface layer and layered AFM in the deeper layers is still lower in energy. In-plane AFM in the surface layer, stabilized by a lower surface energy, has also been found for tetragonal Mn with relaxed in-plane lattice constants of a=3.632 Å and c/a=0.945 (Ref. 7). We note, however, that the constraint to match the larger lattice constant of Rh leads to (i) larger magnetic moments of the surface atoms, (ii) stronger quenching of the moments in the subsurface layer, correlated with (iii) a strong contraction of the distance between first and second subsurface layers, and (iv) a disappearance of the strong buckling of the surface.

TABLE I. Total energy E_{tot} (in eV/atom), energy difference ΔE (in meV/atom), magnetic moments M (in μ_B), changes Δd_{ij} in the interlayer distances with respect to an ideal fcc structure (in %), and Cartesian components σ_x and σ_y of the surface stress (in kbar) for relaxed and unrelaxed Mn(001) surfaces modeled by a 20-layer slab, assuming layered AFM, $c(2\times2)$ in-plane AFM or a mixed magnetic structure with $c(2\times2)$ AFM in the surface layer and layered AFM in the deeper layers.

	$c(2\times2)$ AFM	Layered AFM	Mixed AFM
E_{tot}	−8.8412	−8.8449	−8.8495
ΔE	8.2	4.6	0
Δd_{12}	−15.0	−19.8	−14.1 ± 0.9
Δd_{23}	−29.0	−15.5	−29.0 ± 0.0
Δd_{34}	−11.9	−12.3	−11.5 ± 0.0
Δd_{45}	−12.8	−11.1	−13.9 ± 0.7
$M(\mathrm{Mn}_1)$	±3.42	−3.27	−3.48/3.42
$M(\mathrm{Mn}_2)$	±0.47	1.26	−0.33/0.32
$M(\mathrm{Mn}_3)$	±1.22	−1.95	−1.47/0.61
$M(\mathrm{Mn}_4)$	±2.37	2.24	2.19/2.19
$M(\mathrm{Mn}_5)$	±2.17	−2.20	−2.15/−2.08
σ_x	0.91	−69.06	−63.58
σ_y	−71.40	−69.06	−63.29

Figure 8—for completeness the graph also includes the results for the thinner free-standing films to be discussed below—demonstrates that with increasing thickness of the slab the magnetic energy difference converges indeed to the

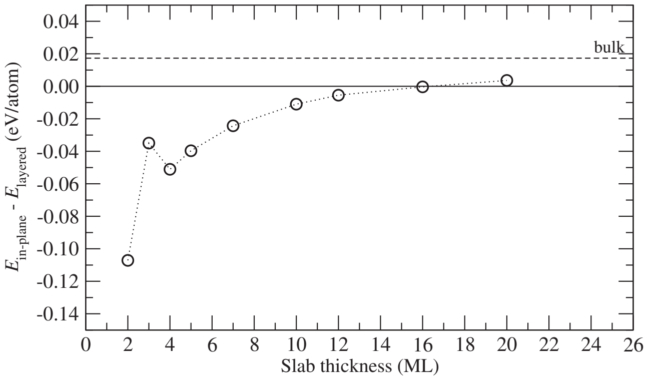

FIG. 8. Magnetic energy difference $E_{\text{in-plane}} - E_{\text{layered}}$ vs slab thickness for slabs of strained tetragonal Mn representing the Mn(001) surface. Cf. text.

bulk value while in thin layers where surface effects dominate in-plane AFM is increasingly favored. At the surface, however, in-plane AFM remains favored because of the energetically unfavorable FM coupling between the strongly enhanced magnetic moments in the surface layer.

C. Mn films on Rh(001)

1. Geometric and magnetic properties

Mn films with one to four and six ML's on a substrate of 10 Rh ML's have been studied in nonmagnetic (NM), in-plane, and layered AFM configurations. The results are compiled in Tables II–IV (Mn layers are counted in roman, Rh layers in arabic numbers). A clean Rh surface undergoes an inward relaxation of the top layer by 3%.

Nonmagnetic Mn is locally stable in an fcc configuration with an atomic volume of 10.7 Å^3 (compared to 11.31 Å^3 for AFM fcc Mn which is 30 meV/atom lower in energy). The larger volume mismatch compared to the Rh(001) substrate is reflected in a strong interlayer contraction in the Mn film which is most pronounced between the top layers and leads to an average axial ratio of $\overline{c/a} \sim 0.8$, closer to a bcc than to an fcc structure. The surface of the Mn film is under compressive stress which increases with increasing thickness of the film. This indicates that the tension caused by the epitaxial constraint is partially reduced by the binding to the substrate. The magnetic energy difference between the NM and the stable $c(2\times2)$ AFM film varies between 94 and 51 meV/Mn-atom.

TABLE II. Total energy, adsorption energy of the Mn overlayer (both in eV/atom), magnetic energy difference relative to the $c(2\times2)$ AFM configuration (in meV/atom), interlayer relaxation Δd_{ij} (in % relative to the interlayer distance in bulk fcc Rh), and Cartesian components $\sigma_x = \sigma_y$ (in kbar) for nonmagnetic Mn/Rh(001) films. Mn layers are numbered I–VI, relaxed Rh layers 1–3.

	1 ML	2 ML	3 ML	4 ML
E_{tot}	−7.1758	−7.3435	−7.4595	−7.5664
E_{ads}	−1.02	−1.81	−1.48	−1.58
ΔE	94.0	51.4	55.7	58.4
$\Delta d_{\text{III/IV}}$				−37.4
$\Delta d_{\text{II/III}}$			−36.7	−13.1
$\Delta d_{\text{I/II}}$		−35.6	−12.2	−26.0
$\Delta d_{\text{I/1}}$	−18.3	−0.6	−11.9	−5.1
$\overline{c/a}$	0.817	0.814	0.797	0.796
$\Delta d_{1/2}$	8.3	1.1	5.2	2.6
$\Delta d_{2/3}$	−1.1	0.5	0.0	0.1
σ_x	−11.2	−12.1	−16.4	−17.0

Layered AFM Mn/Rh(100) films have a magnetic profile similar to that calculated for the surface of strained tetragonal Mn in the same magnetic configuration, although the oscillatory variation of the magnetic moments is more pronounced, caused by an enhanced magnetic moment of the Mn interface layer. The magnetic overlayer also induces a weak magnetic polarization of the substrate. The Mn/Rh coupling at the interface is always antiferromagnetic (in contrast to Fe/Rh(001) films where the interface coupling is ferromagnetic[50]) but longer-range exchange interactions lead to a higher induced moment in the second Rh layer than at the interface. The profile of the interlayer distances is also only weakly influenced by the substrate although the Mn/Rh binding is quite strong as demonstrated by a binding energy of −1.7 eV/atom for the first Mn ML. The binding energies listed in the tables are calculated as the total energy of a film/substrate complex with n Mn monolayers minus the sum of the total energies of a $(n-1)$-ML Mn/Rh(001) film plus a free-standing Mn ML. The binding energy of the first Mn ML is −1.71 eV/atom, it is smaller by 0.2 eV/atom for the second ML and increases again to −1.61 eV for slabs with 3 to 6 ML.

The average axial ratio of films with two to six monolayers is $\overline{c/a} = 0.875 \pm 0.01$, to be compared to $\overline{c/a} = 0.856$ as calculated for the relaxed part of a thick slab representing the (001) surface of strained tetragonal Mn. The distance between the uppermost Rh layers is expanded by about 2%—this shows that the strong binding through the interface overcompensates the surface-induced contraction found on a clean Rh(001) surface. The surface tension calculated for the supported films with 2 to 4 ML's is lower by nearly 1 order of magnitude than on the surface of strained Mn, only for a 6 ML film it increases to about half this value. This demonstrates that the strong film/substrate coupling efficiently stabilizes the thinner films, while for thicker films the surface is under considerable compressive stress.

For completeness, the results compiled in Table III also include a single, ferromagnetic Mn ML on Rh(001). The magnetic moments of 3.76 μ_B in the FM Mn film is only slightly lower than in a freestanding ML and the largest moment calculated so far for a square supported ML of Mn. Evidently the formation of a large moment is favored by the strong lateral extension imposed by the coupling to the Rh substrate and an only modest contraction of the Mn/Rh interlayer distance.

In-plane $c(2\times2)$ AFM is energetically favored over layered AFM for all films, the magnetic energy difference of about 19 meV/atom remains almost the same for films with 2 to 6 ML's. For films consisting of 2 and 3 ML's the binding of the added Mn layer is weaker than for a layered AFM

TABLE III. Total energy, adsorption energy of the Mn overlayer (both in eV/atom), magnetic energy difference relative to the $c(2\times 2)$ AFM configuration (in meV/atom), interlayer relaxation Δd_{ij} (in % relative to the interlayer distance in bulk fcc Rh), average axial ratio $\overline{c/a}$ of the tetragonal Mn film, magnetic moments (in μ_B), and Cartesian components $\sigma_x = \sigma_y$ (in kbar) for layered AFM Mn/Rh(001) films (the monolayer film is ferromagnetic). Mn layers are numbered I–VI, relaxed Rh layers 1–3.

	1 ML (FM)	2 ML	3 ML	4 ML	6 ML
E_{tot}	−7.2385	−7.3753	−7.4989	−7.6049	−7.8447
E_{ads}	−1.71	−1.51	−1.61	−1.61	
ΔE	31.3	19.7	16.4	19.9	18.8
$\Delta d_{\mathrm{V/VI}}$					−19.7
$\Delta d_{\mathrm{IV/V}}$					−15.8
$\Delta d_{\mathrm{III/IV}}$				−19.9	−13.9
$\Delta d_{\mathrm{II/III}}$			−19.2	−15.4	−12.2
$\Delta d_{\mathrm{I/II}}$		−20.5	−14.2	−11.0	−12.1
$\Delta d_{\mathrm{I/1}}$	−7.6	−5.1	−4.0	−3.3	−4.8
$\overline{c/a}$	0.924	0.872	0.875	0.876	0.882
$\Delta d_{1/2}$	3.4	2.3	1.8	1.8	2.3
$\Delta d_{2/3}$	−0.1	0.4	0.5	0.4	0.5
M(MnVI)					−3.28
M(MnV)					1.22
M(MnIV)				−3.27	−1.85
M(MnIII)			3.27	1.28	2.09
M(MnII)		−3.23	−1.49	−1.97	−2.18
M(MnI)	3.76	1.51	2.25	2.86	2.46
M(Rh1)	0.17	−0.03	−0.09	−0.03	−0.04
M(Rh2)	−0.12	−0.14	−0.17	−0.17	−0.17
M(Rh3)	−0.04	0.00	0.02	0.00	0.00
σ_x	10.5	−3.1	−7.3	−7.3	−25.4

film—the weaker binding reduces the strong energetic preference for in-plane AFM found in the free-standing films which remains, however, the magnetic configuration with the lowest energy in all Mn/Rh(001) films covered by this study. For 4 and 6 ML films the geometric and magnetic profile is very similar to that found for the surface of strained tetragonal Mn in the same magnetic configuration: high surface moments of about 3.4 μ_B, strongly reduced moments in the subsurface Mn layer, coupled to a very strong interlayer distance. However, the Mn moments are also enhanced through the contact with the Rh substrate and this leads to a less pronounced magnetic quenching in the subsurface layers and a more modest interlayer contraction for 2 and 3 ML films. As a consequence, the average axial ratio of the tetragonal Mn film shows a more pronounced variation with increasing thickness than for layered AFM. Because the in-plane AFM films are magnetically compensated, the magnetic moments induced in the Rh substrate are very small, except in the monolayer limit.

For the 6 ML film we have also investigated the stability of a mixed AFM configuration with in-plane AFM in the surface layer and layered AFM in the deeper layers (see Table IV). Although this configuration is 4.6 meV/Mn atom lower in energy than the film with layered AFM, it is still 14.2 meV/Mn atom higher than the film with in-plane AFM in all six layers. The stability of in-plane $c(2\times 2)$ AFM not only at the surface but through the entire multilayer films of Mn on Rh(001) is a remarkable result contrasting previous findings for Mn films on other substrates. On a Cu(001) surface, in-plane AFM is stable only in the monolayer limit, already for a bilayer film layered AFM is preferred.[16] On a ferromagnetic Fe(001) substrate in-plane AFM is preferred in monolayer and bilayer films, in thicker Mn films, the ground state configuration predicted by the calculations combines in-plane $c(2\times 2)$ surface magnetism with layered AFM in the deeper layers.[7] On a W(001) substrate monolayer and bilayer Mn films are ferromagnetic (the unusual magnetic configuration being stabilized by the large strains and the strong hybridization with the substrate) but already in a 3 ML film in-plane AFM represents the ground state.[24]

2. Island formation

Under the assumption that islands formed on the surface of the film are sufficiently large such that contributions to the total energy from the step edges and side facets of the islands are negligible, the energy for the decomposition of a flat film consisting of $(n+1)$ ML's into a n-ML-thick basis layer and islands with a step height of m ML's is given by $\Delta E_{isl}^{m,n} = [(m-1)E_{n\mathrm{Mn/Rh}} + E_{(m+n)\mathrm{Mn/Rh}} - mE_{(n+1)\mathrm{Mn/Rh}}]/m$ with negative values indicating a tendency to island formation.

The results compiled in Table V show that the tendency to island formation is strongly influenced by the magnetic prop-

TABLE IV. Total energy, adsorption energy of the Mn overlayer (both in eV/atom), interlayer relaxation Δd_{ij} (in % relative to the interlayer distance in bulk fcc Rh), average axial ratio $\overline{c/a}$ of the tetragonal Mn film, magnetic moments (in μ_B), and Cartesian components σ_x and σ_y (in kbar) for $c(2\times2)$ in-plane AFM Mn/Rh(001) films). Mn layers are numbered I–VI, relaxed Rh layers 1 to 3. For a 6 ML film results are also given for in-plane $c(2\times2)$ AFM ordering in the surface, followed by layered AFM in the deeper layers. Cf. text.

	1 ML	2 ML	3 ML	4 ML	6 ML	6 ML
	In-plane $c(2\times2)$ AFM					Mixed AFM
E_{tot}	−7.2698	−7.3949	−7.5152	−7.6248	−7.8635	−7.8493
E_{ads}	−2.06	−1.40	−1.58	−1.67		
$\Delta d_{\mathrm{V/VI}}$					−15.1	−14.1 ± 0.8
$\Delta d_{\mathrm{IV/V}}$					−29.1	−28.9 ± 0.0
$\Delta d_{\mathrm{III/IV}}$				−14.8	−13.8	−12.3 ± 0.0
$\Delta d_{\mathrm{II/III}}$			−17.6	−29.2	−15.2	−14.7 ± 0.7
$\Delta d_{\mathrm{I/II}}$		−5.2	−12.7	−6.6	−7.0	−11.0 ± 0.7
$\Delta d_{\mathrm{I/1}}$	−9.9	−9.5	−6.7	−7.7	−7.6	−4.5 ± 0.1
$\overline{c/a}$	0.901	0.926	0.877	0.854	0.854	0.858
$\Delta d_{1/2}$	4.3	4.6	3.1	3.5	3.6	2.3 ± 0.1
$\Delta d_{2/3}$	−0.3	0.1	0.3	0.2	0.2	0.7 ± 0.1
M(MnVI)					±3.41	−3.49/3.41
M(MnV)					±0.45	0.27/0.34
M(MnIV)				±3.43	±1.19	−1.39/0.66
M(MnIII)			±3.20	±0.38	±2.06	2.11/2.08
M(MnII)		±3.61	±1.45	±1.37	±2.29	−2.14/−2.07
M(MnI)	±3.59	±2.68	±2.62	±2.82	±2.81	2.54/2.53
M(Rh1)	±0.07	±0.01	±0.02	±0.01	±0.01	−0.4/−0.06
M(Rh2)	±0.05	±0.04	±0.03	±0.01	±0.01	−0.18/−0.18
M(Rh3)	±0.02	±0.01	±0.01	±0.01	±0.01	−0.1/0.00
σ_x	5.2	1.4	−3.1	−1.6	−3.3	−19.3
σ_y	5.2	−8.5	−13.6	−5.3	−19.4	−19.3

erties of the films. While non-magnetic Mn ML is unstable with respect to decomposition into 2-ML- or 3-ML-high islands, AFM ML's are stable. The situation is reversed for 2 ML films: NM films are stable while for both types of AFM films the decomposition into 2-ML-high islands based on a compact monolayer is energetically favorable. For $c(2\times2)$ in-plane AFM and NM films consisting of 3 ML's island formation is also favored, films with a layered AFM are marginally stable.

The marked difference in the stability of Mn monolayers against island formation is a consequence of the interplay of magnetism and chemical bonding in Mn. In the absence of exchange splitting the Mn d band is half-filled, the almost exclusive occupation of bonding states maximizes the Mn-Mn bond strength. On the other hand the asymmetric form of the Mn d DOS reduces the Mn d-Rh d overlap and hence the strength of the Mn-Rh bonding [see Fig. 9(a)]. As a consequence, the gain of Mn-Mn bond energy on island formation out weights the loss of Mn-Rh bonding and island formation is favored.

In a ferromagnetic or in-plane antiferromagnetic state on the other hand the majority Mn d states are almost completely filled—the occupation of both bonding and antibonding states minimizes the Mn-Mn bond strength. The shift of the Mn d majority states to higher binding energies also increases the Mn d-Rh d overlap [see Figs. 9(b) and 9(c)], promoting a strong binding across the Mn-Rh interface and stabilizing a compact overlayer.

3. Energetics of intermixing at the interface

The Mn-Rh phase diagram demonstrates that alloying is energetically favorable in the bulk although perhaps kinetically hindered during film growth. We have examined the formation of an ordered mixed $\mathrm{Mn}_{0.5}\mathrm{Rh}_{0.5}$ bilayer at the Mn/Rh interface. Within this bilayer Mn and Rh atoms are arranged in a $c(2\times2)$ pattern. For a single Mn layer on Rh(001) intermixing with an AFM coupling within the bilayer is energetically favored by 160 meV/atom over a compact Mn ML with $c(2\times2)$ in-plane AFM. If one or two Mn ML's with in-plane AFM are added on top of the AFM bilayer, the energy gain by intermixing increases even to 338 meV/atom and 224 meV/atom, respectively, compared to an in-plane AFM 2 ML film. The contraction of the distance between the two Mn layers is about the same as in the absence of intermixing but the overall tetragonal axial ratio in the Mn-containing layers is somewhat closer to unity be-

TABLE V. Island formation energies $\Delta E_{isl}^{m,n}$ (in meV/surface atom) for the decomposition of an $(n+1)$-ML-thick films into a n ML basis layer covered by m-ML-high islands, calculated for nonmagnetic and layered and in-plane AFM islands.

m	$n=0$	$n=1$	$n=2$
	NM		
2	−396	168	−52
3	−415	190	
	Layered AFM		
2	104	−51	0
3	104	−69	
	In-plane AFM		
2	330	−94	−45
3	377	−155	

cause the distance between the intermixed layers is almost the same as in the Rh substrate. Figure 10 summarizes the calculated tetragonal distortion of the fct Mn/Rh(001) in different magnetic configurations and with and without intermixing.

4. Activation energy for adsorbate/substrate exchange processes

Although we find the formation of an intermixed interface layer to be energetically favored by about 0.15–0.35 eV/atom, intermixing may be kinetically hindered at low temperatures. To examine this question, we have calculated the barrier for the exchange process between a Mn adatom and an atom for the Rh substrate using the nudged elastic band technique.[51]

For the calculations of the activation barrier of such an exchange process we have used six-layer slabs with a 5×5 surface cell, separated by a vacuum layer of 15 Å. Together with the adatom there are 151 atoms per cell. Brillouin-zone sampling has been restricted to the Γ point. In the initial configuration a Mn atom is located in a fourfold hollow at a relaxed height of 1.69 Å above the surface layer (reduced by 11.7% compared to the bulk interlayer distance). The Mn atom is strongly bound to the substrate, the adsorption energy (relative to the clean Rh surface and an isolated spin-polarized Mn atom) is −4.04 eV. Although the binding of the isolated Mn atom is very strong, it induces only a very modest buckling of the substrate, the four nearest-neighbor Rh atoms relax outward by 0.027 Å.

We find an activation energy of 0.99 eV, in the transition state the Mn atom is located roughly at a bridge position. The two nearest-neighbor Rh atoms relax sideways, the potential-energy profile for the exchange process is slightly asymmetric. In the final state the Mn atom occupies a lattice site in the surface layer, relaxed outward by 0.075 Å relative to the average z coordinates of the surrounding Rh atoms. The Rh atom pushed out of the surface occupies a hollow site, at a height of 1.648 Å (also reduced by 13.7% compared to the bulk interlayer distance). A remarkable result is that the total energy of this configuration is by 0.08 eV higher than that of the initial configuration with the Mn adatom. In the present context the important result is that due to the high activation energy, intermixing is kinetically hindered at least up to room temperature. The energy gain upon formation of a 50/50 mixed interface layer depends on the formation of an ordered alloy phase. However, we should also point out that

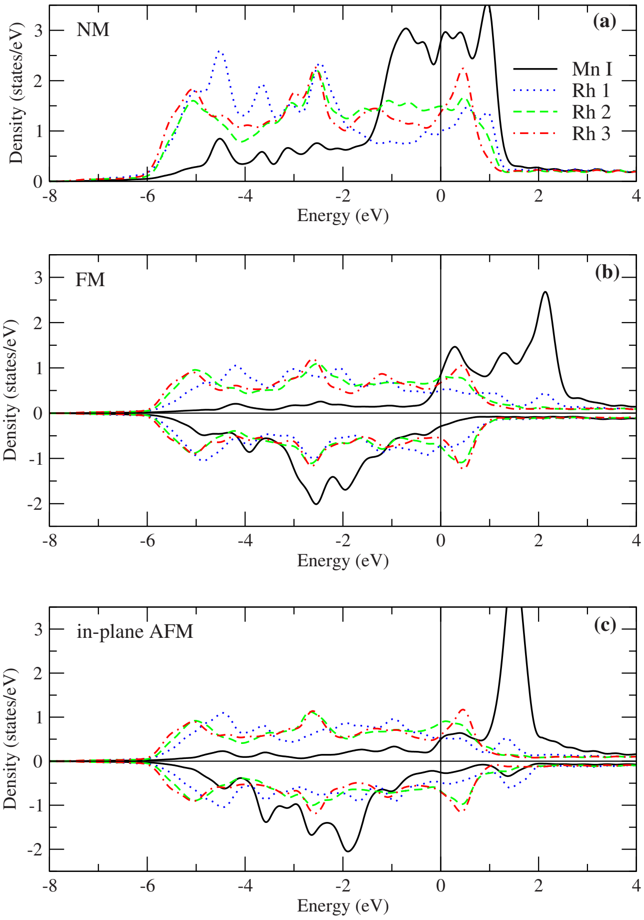

FIG. 9. (Color online) Layer-resolved local DOS for Mn monolayers on Rh(001). (a) Nonmagnetic Mn and [(b) and (c)] spin-polarized DOS for ferromagnetic and $c(2\times2)$ in-plane antiferromagnetic Mn monolayers. Cf. text.

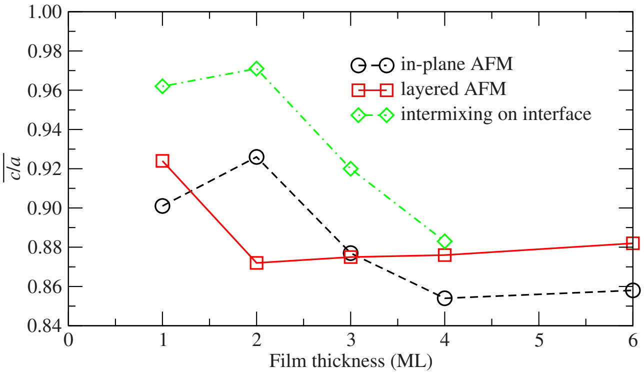

FIG. 10. (Color online) Average c/a ratio for fct Mn/Rh(001) as a function of film thickness. Cf. text.

for intermixing at step edges, the activation energy will be lower than for the exchange process on the flat terraces.

IV. DISCUSSION AND CONCLUSIONS

Our STM measurements provide information on the structure of Mn films supported on Rh(001) substrates with spatial resolution, including film-substrate intermixing, the temperature dependence of the growth mode, and the thickness-dependent apparent axial ratio both for open and closed film morphologies.

Detailed *ab initio* DFT calculations have been performed for fct Mn strained to match the in-plane lattice constant of Rh(001), as well as for free-standing Mn layers and thin films supported on Rh(001). The calculations highlight the important role of magnetism in determining the structure of fct Mn in the bulk, at the surface, and in thin films. The strong surface-induced increase in the magnetic moments of Mn atoms in the surface layer leads to an antiferromagnetic ordering which is different at the surface and in the bulk. Bulk fct Mn with an axial ratio $c/a \leq 1$ shows layered antiferromagnetism while the dominant in-plane exchange coupling leads to the formation of in-plane $c(2\times2)$ antiferromagnetism in the surface layer. Surface and bulk are partially decoupled by subsurface layers with strongly quenched magnetic moments. In thin films, in-plane $c(2\times2)$ antiferromagnetism of the entire film remains dominant up to a thickness of at least six monolayers, in contrast to the predictions for Mn films grown on other cubic substrates where layered AFM is stabilized already for films thicker than two or three monolayers, at least in the subsurface layers. Magnetic ordering is coupled to strong magnetovolume effects hence magnetism also influences the growth and structure of the films. In particular we find:

(a) *sub-ML films*—the initial Mn monolayer is very stable with respect to formation of 2 ML islands on the clean Rh surface, i.e., the wetting of the substrate by the first Mn monolayer is perfect. The calculations predict a nonmagnetic Mn ML to be unstable against island formation while a magnetically ordered Mn film is found to be stable. The reason is the peculiar spin-polarized electronic structure of the magnetically ordered first Mn monolayer in whose nearly completely filled majority *d* band both bonding and antibonding states are occupied, minimizing the strength of the Mn-Mn interaction, while allowing a large overlap of the Rh and Mn *d* bands and promoting a strong Rh-Mn binding. This destabilizes the 2 ML islands relative to a compact monolayer. In films with three and more monolayers a lower Mn moment in the deeper layers allows again for a stronger Mn-Mn binding (cf. Sec. III C 2). The weak Mn-Mn interaction, accompanied by compressive surface stress (cf. Table IV), provides also an explanation for the observed low two-dimensional cohesion of the Mn islands in the sub-ML films leading to fluctuating ML-island shapes due to mobile step edge atoms. In this context, the Mn vacancies and ⟨100⟩-aligned island edges may be explained as a tendency to reduce the average number of Mn neighbor atoms. This shift of bond strength from Mn-Mn to Mn-Rh bonding is also a signature of the pronounced tendency to form strongly magnetic fcc-like Mn-Rh intermetallic compounds (cf. Sec. III C 3).

(b) *2-ML films*—the reason for the observed instability of the second ML toward formation of many-ML islands is the mentioned frustration of the 2 ML films between high moments and high Mn-Mn bond strengths. With every further ML, however, the frustration is gradually removed by forming weak to moderate moments in the center layers between the high moment interface and surface layers. As $\overline{c/a}$ ratio (Table IV) and island formation energy (Table V) are correlated, the observed 2 ML instability should be accompanied by a change in the apparent $\overline{c/a}$ ratio in good agreement with experiment (cf. Fig. 4). With decreasing frustration and increasing stability of thicker films also the driving force toward three-dimensional growth decreases and the films eventually return to two-dimensional growth in agreement with the low surface energy of fct Mn(001) (1.16 eV/atom for layered AFM, 1.06 eV/atom if in-plane AFM is admitted in the surface layer)[7] compared to 1.44 eV/atom for a Rh(001) surface.[52] Note that while the instability of 2-ML-thick films is predicted for both in-plane and layered AFM, the high volume of locally 2–3-ML-thick films suggested by the apparent height measurements is specific to the in-plane AFM configuration (Fig. 10).

(c) *Atomic volume and tetragonal ratio up to 20 ML*—considering a wider thickness range, the in-plane AFM model calculations predict a large average $\overline{c/a}$ ratio of 0.92 in 1 and 2 ML films but already the same value (0.85) as an infinitely thick epitaxial Mn film at 4 ML thickness. This agrees qualitatively with the measured apparent height differences [cf. Figs. 4(c) and 6], which are consistent with a more or less continuous drop of the $\overline{c/a}$ ratio from ≈1.0 in 2 ML films to 0.94 ± 0.02 in films thicker than 8 ML. Based on the tunneling spectra, however, electronic contributions to the apparent height differences cannot be completely ruled out in the 1–3 ML thickness range (cf. Sec. II D). The films grow epitaxially at least up to 20 ± 3 ML thickness without forming mismatch reconstructions and the epitaxial strain is estimated to be less than 1%.

The continuous variation in the $\overline{c/a}$ ratio as a function of film thickness contrasts a discontinuous fcc→fct structural transition reported for Mn films on $Cu_3Au(001)$ at 8–14 ML thickness,[28,29] although the in-plane lattice constant of this substrate is not very different to that of Rh. The atomic volume of the fcc phase is about 7% larger than for the fct phase[28]—this difference is about the same as between the bulk phases of α- and γ-Mn. Magneto-optic Kerr-effect measurements on $Mn/Cu_3Au(001)$ films show the absence of any hysteresis for clean Mn films but a strong exchange bias in $Fe/Mn/Cu_3Au$ persisting up to temperatures ranging between 220 and 300 K, depending on the thickness of the Mn film.[29] These observations are compatible with antiferromagnetic ordering of the Mn films. Moreover, the absence of such a discontinuous transition in Mn/Rh(001) films shows that it is not an intrinsic property of ultrathin fct Mn films. The phase change and reconstruction phenomena observed in Mn/Cu_3Au films must be related either to interface intermixing or to the 1.6% smaller lattice constant of $Cu_3Au(001)$ with respect to Rh(001).

The overestimation of the size ratio of Rh and Mn in DFT calculations remains a challenge and should be kept in mind in confronting theory and experiment. We have pointed out that with all currently available exchange-correlation functionals, DFT tends to overestimate the size mismatch between Rh and Mn even if antiferromagnetic ordering is taken into account. For nonmagnetic Mn, DFT predicts an even smaller volume, increasing the discrepancy between theory and experiment. However, it has to be emphasized that the paramagnetic phase of Mn above the Néel temperature should be described as a disordered local moment phase with local paramagnetic moments which are only slightly reduced compared to those of the antiferromagnetic phase. Very recently it has been suggested that the underestimation of the equilibrium volume for all magnetic $3d$ elements arises from a neglect of strong electronic correlations caused by intra-atomic Coulomb repulsions. If these correlations are treated within a dynamical mean-field theory,[53] the equilibrium volume increases by 17–28 % with respect to the local density approximation value for Coulomb repulsion between $U=2.6$ and 3.0 eV. This means that the corrections are slightly larger than those provided by gradient corrections to the exchange-correlation functional but strong sensitivity to the precise value of U suggests further investigations.

ACKNOWLEDGMENT

This work has been supported by the Universität Wien through the VASP project.

---

*Present address: Aalto University, Espoo, Finland. zeleny@cc.hut.fi

†Present address: Ecole Polytechnique Fédérale de Lausanne, Lausanne, Switzerland.

‡albert.biedermann@univie.ac.at

§juergen.hafner@univie.ac.at

[1] A. C. Lawson, A. C. Larson, M. C. Aronson, S. Johnson, Z. Fisk, P. C. Canfield, J. D. Thompson, and R. B. von Dreele, J. Appl. Phys. **76**, 7049 (1994).

[2] M. O'Keeffe and S. Andersson, Acta Crystallogr., Sect. A: Cryst. Phys., Diffr., Theor. Gen. Crystallogr. **33**, 914 (1977).

[3] H. Fujihisa and K. Takemura, Phys. Rev. B **52**, 13257 (1995).

[4] D. Hobbs, J. Hafner, and D. Spišák, Phys. Rev. B **68**, 014407 (2003).

[5] J. Hafner and D. Hobbs, Phys. Rev. B **68**, 014408 (2003).

[6] T. Oguchi and A. J. Freeman, J. Magn. Magn. Mater. **46**, L1 (1984).

[7] J. Hafner and D. Spišák, Phys. Rev. B **72**, 144420 (2005).

[8] P. Mohn, K. Schwarz, M. Uhl, and J. Kübler, Solid State Commun. **102**, 729 (1997).

[9] Y. Endoh and Y. Ishikawa, J. Phys. Soc. Jpn. **30**, 1614 (1971).

[10] O. Rader, W. Gudat, C. Carbone, E. Vescovo, S. Blügel, R. Kläsges, W. Eberhardt, M. Wuttig, J. Redinger, and F. J. Himpsel, Phys. Rev. B **55**, 5404 (1997).

[11] W. F. Egelhoff, I. Jacob, J. M. Rudd, J. F. Cochran, and B. Heinrich, J. Vac. Sci. Technol. A **8**, 1582 (1990).

[12] D. Tian, S. C. Wu, F. Jona, and P. M. Marcus, Solid State Commun. **70**, 199 (1989).

[13] S. Andrieu, H. M. Fischer, M. Piecuch, A. Traverse, and J. Mimault, Phys. Rev. B **54**, 2822 (1996).

[14] R. Wu and A. J. Freeman, Phys. Rev. B **51**, 17131 (1995).

[15] T. Asada and S. Blügel, Physica B **237-238**, 359 (1997).

[16] M. Eder, J. Hafner, and E. G. Moroni, Phys. Rev. B **61**, 11492 (2000).

[17] J. T. Kohlhepp and W. J. M. de Jonge, Phys. Rev. Lett. **96**, 237201 (2006).

[18] T. K. Yamada, M. M. J. Bischoff, G. M. M. Heijnen, T. Mizoguchi, and H. van Kempen, Phys. Rev. Lett. **90**, 056803 (2003).

[19] U. Schlickum, N. Janke-Gilman, W. Wulfhekel, and J. Kirschner, Phys. Rev. Lett. **92**, 107203 (2004).

[20] C. Grazioli, D. Alfé, S. R. Krishnakumar, S. S. Gupta, M. Veronese, S. Turchini, N. Bonini, A. DalCorso, D. D. Sarma, S. Baroni, and C. Carbone, Phys. Rev. Lett. **95**, 117201 (2005).

[21] S. Andrieu, M. Finazzi, Ph. Bauer, H. Fischer, P. Lefevre, A. Traverse, K. Hricovini, G. Krill, and M. Piecuch, Phys. Rev. B **57**, 1985 (1998).

[22] E. C. Passamani, B. Croonenborghs, B. Degroote, and A. Vantomme, Phys. Rev. B **67**, 174424 (2003).

[23] C. L. Gao, U. Schlickum, W. Wulfhekel, and J. Kirschner, Phys. Rev. Lett. **98**, 107203 (2007).

[24] S. Dennler and J. Hafner, Phys. Rev. B **72**, 214413 (2005).

[25] P. Ferriani, S. Heinze, G. Bihlmayer, and S. Blügel, Phys. Rev. B **72**, 024452 (2005).

[26] P. Ferriani, K. von Bergmann, E. Y. Vedmedenko, S. Heinze, M. Bode, M. Heide, G. Bihlmayer, S. Blügel, and R. Wiesendanger, Phys. Rev. Lett. **101**, 027201 (2008).

[27] B. Predel, *Physical Chemistry*, Landolt-Börnstein, Group IV Vol. 5H (Springer, Berlin, 1997).

[28] B. Schirmer, B. Feldmann, A. Sokoll, Y. Gauthier, and M. Wuttig, Phys. Rev. B **60**, 5895 (1999).

[29] W. C. Lin, T. Y. Chen, L. C. Lin, B. Y. Wang, Y. W. Liao, K.-J. Song, and M.-T. Lin, Phys. Rev. B **75**, 054419 (2007).

[30] P. T. Wouda, B. E. Nieuwenhuys, M. Schmid, and P. Varga, Surf. Sci. **359**, 17 (1996).

[31] P. J. Cumpson and M. P. Seah, Surf. Interface Anal. **25**, 430 (1997).

[32] The best high pass filter radius r is determined by maximizing both the signal-to-noise ratio $s \propto \sigma''(h)/\sigma$ and the efficiency of the background subtraction $b \propto sr^{-1/2}$ (with b nearly independent of r in absence of background). Maximizing their geometric average $(bs)^{1/2}=sr^{-1/4}$ with respect to r provides a useful balance between noise reduction and background correction.

[33] H. W. King, in *CRC Handbook of Chemistry and Physics*, 82nd ed., edited by D. R. Lide (CRC Press, Boca Raton, 2001).

[34] J. E. Demuth and T. N. Rhodin, Surf. Sci. **45**, 249 (1974).

[35] C. O. S. Sorzano, P. Thevenaz, and M. Unser, IEEE Trans. Biomed. Eng. **52**, 652 (2005).

[36] J. W. Matthews and J. L. Crawford, Thin Solid Films **5**, 187 (1970).

[37] B. Müller, B. Fischer, L. Nedelmann, A. Fricke, and K. Kern, Phys. Rev. Lett. **76**, 2358 (1996).

[38] A. Klein, W. Meyer, A. Schmidt, B. Gumler, S. Müller, L. Ham-

mer, and K. Heinz, Phys. Rev. B **78**, 045422 (2008).

[39] G. Kresse and J. Furthmüller, Phys. Rev. B **54**, 11169 (1996); Comput. Mater. Sci. **6**, 15 (1996).

[40] P. E. Blöchl, Phys. Rev. B **50**, 17953 (1994).

[41] G. Kresse and D. Joubert, Phys. Rev. B **59**, 1758 (1999).

[42] M. Methfessel and A. T. Paxton, Phys. Rev. B **40**, 3616 (1989).

[43] V. Fiorentini and M. Methfessel, J. Phys.: Condens. Matter **8**, 6525 (1996).

[44] J. P. Perdew, K. Burke, and M. Ernzerhof, Phys. Rev. Lett. **77**, 3865 (1996); **78**, 1396(E) (1997).

[45] P. Villars and L. D. Calvert, *Pearson's Handbook of Crystallographic Data for Intermetallic Phases*, 2nd ed. (ASM International, Materials Park, Ohio, 1991).

[46] T. Asada and K. Terakura, Phys. Rev. B **47**, 15992 (1993).

[47] J. P. Perdew, J. A. Chevary, S. H. Vosko, K. A. Jackson, M. R. Pederson, D. J. Singh, and C. Fiolhais, Phys. Rev. B **46**, 6671 (1992); **48**, 4978(E) (1993).

[48] J. P. Perdew, A. Ruzsinszky, G. I. Csonka, O. A. Vydrov, G. E. Scuseria, L. A. Constantin, X. Zhou, and K. Burke, Phys. Rev. Lett. **101**, 239702 (2008).

[49] R. Armiento and A. E. Mattsson, Phys. Rev. B **72**, 085108 (2005).

[50] D. Spišák and J. Hafner, Phys. Rev. B **73**, 155428 (2006).

[51] G. Henkelman and H. Jónsson, J. Chem. Phys. **111**, 7010 (1999).

[52] A. Eichler, J. Hafner, J. Furthmüller, and G. Kresse, Surf. Sci. **346**, 300 (1996).

[53] I. Di Marco, J. Minár, S. Chadov, M. I. Katsnelson, H. Ebert, and A. I. Lichtenstein, Phys. Rev. B **79**, 115111 (2009).